Performance Assessment of a Portable Mass Spectrometer Using a Linear Ion Trap Operated in Non-Scanning Mode

Aurika Janulyte[1*], Yves Zerega[1], Jacques Andre[1], Boris Brkic[2,3] and Stephen Taylor[3]

[1]Aix-Marseille Université, LISA EA 4672, Campus Etoile - Service 461, 52 Avenue Escadrille Normandie Niémen, 13397 Marseille Cedex 20, France

[2]Q-Technologies Ltd, 100 Childwall Road, Liverpool L15 6UX, United Kingdom

[3]University of Liverpool, Department of Electrical Engineering and Electronics, Brownlow Hill, Liverpool L69 3GJ, United Kingdom

Correspondence to: Aurika JANULYTE, Aix-Marseille Université, LISA EA 4672, Campus Etoile Service 461, 52 Avenue Escadrille Normandie Niémen, 13397 Marseille Cedex 20, France.
E-mail: aurika.janulyte@univ-amu.fr

ABSTRACT

RATIONALE: The desire for mass spectrometer portability provides the motivation for simpler, lighter electronics to deliver switched potentials applied to the electrodes of the linear ion trap operated in non-scanning mode. Using a novel method of modelling and theoretical analysis, we simulate the mass analyser performance in these unfavourable operating conditions.

METHODS: The electrical fields are simulated using the Charge Particle Optics software which employs the boundary element method. The ion trajectories are computed from the ion cage of the EI source to the interior of the trap where the ions are confined. The spatial/temporal ion distributions during injection are calculated from the individual ion trajectories computed with constant time-steps. Due to geometric non-linearities, $\beta_y = 0$ lines close to the apex of the stability diagram have been computed for different initial positions with zero initial velocities in order to define the acceptable maximum axial extension.

RESULTS: The DC potential well depth has been estimated at about 15 eV from the axial velocity

distribution, and the minimum time of ion injection at 120 μs from the temporal ion distribution. To ensure a mass separation of one unit and the confinement of the whole of the injected ions, buffer gas cooling is necessary to reduce the trajectory excursion amplitudes to 0.1 and 15 mm in the radial and axial directions, respectively.

CONCLUSIONS: The portable mass spectrometer is predicted to achieve a mass resolution of better than one mass unit providing that He buffer gas is used. An additional cooling sequence has to be added prior to moving the operating point toward the apex.

KEYWORDS

Portable Mass Spectrometer; Linear Ion Trap; Non-scanning Operating Mode; Non-linearity influence on mass-resolution.

INTRODUCTION

There are various configurations of 2D ion traps, or linear ion traps (LIT). The ideal quadrupole device has a structure with hyperbolic profile electrodes (rods), each rod being cut into three axial sections[1-5], while the simplest structure is obtained with a lens placed at each end of four hyperbolic rods.[6, 7] The DC potential applied to the front and back sections (hyperbolic electrodes or lenses) allows the electrostatic confinement of the ions along the z-direction, in addition to the electrodynamic confinement in the radial plane.

It is often assumed that the expression for the potential in the LIT can be separated into two parts. This assumption is most accurate when the linear trap is composed of three sets of rod electrodes. The first potential, $\Phi_{QMF}(x,y,t)$, is applied to the four rods (as for a Quadrupole Mass Filter, QMF), and the second $\Phi_{DC}(x,y,z)$ is the DC potential applied to both end sections/lenses.

Different potential configurations can be employed to maintain the ions in the radial plane (Table 1). Configuration No. 1 is the standard confinement potential configuration. The potential $V(t)=U_0+V_0\cos\Omega t$ (where U_0 is the DC potential, V_0 the RF zero-to-peak amplitude and Ω the angular frequency of the RF potential) is applied to the pair of opposite electrodes in the x-direction and $-V(t)$ is applied to the pair of opposite electrodes in the y-direction.

For a portable device, it would be preferable to use a single RF power supply. In the configuration No. 3, the potential $V(t)$ is applied to the pair of opposite electrodes in the y-direction, while the pair of opposite electrodes in the x-direction are grounded. This configuration is

not of interest as the centre of the trap is always at U_0 and can cause a dispersion of the ions at injection. In configuration No. 2, the potential $V(t)$ is applied to the pair of opposite electrodes in the y-direction and the DC potential U_0 is applied to the pair of opposite electrodes in the x-direction. Over a period of the RF voltage waveform, the average value of the potential in the centre of the trap is zero.

In the radial plane, the ion motion equations can be described by a Mathieu equation:

$$\frac{d^2u}{d\tau^2} + (a_u - 2q_u \cos 2\tau)u = 0 \qquad (1)$$

using the reduced parameters (for instance, for configuration No. 1):

$$\begin{aligned} a_x &= -a_y = \frac{8zeU_0}{mr_0^2\Omega^2} \\ a_x &= -a_y = \frac{-4zeV_0}{mr_0^2\Omega^2} \\ 2\tau &= \Omega t \end{aligned} \qquad (2)$$

with r_0, the smallest distance separating the hyperbolic rod electrodes from the central axis of the LIT, m/z the mass-over-charge ratio of the ion and e the charge of the electron.

The potential induced by the two end-caps is often expressed by:[8, 9]

$$\Phi_{DC}(x,y,z) = C + \frac{kU_e}{z_0^2}\left[z^2 - \frac{x^2+y^2}{2}\right] + \ldots \qquad (3)$$

where U_e is the potential applied to both end-electrodes. In this expression, the resulting potential is limited to the quadrupole order term and a value different from zero in the centre of the trap is taken into account. Using $\Phi_{QMF}(x,y,t) + \Phi_{DC}(x,y,z)$ as the solution of the Laplace equation, the ion motion equation leads to a stability diagram different from that of the quadrupole mass filter. The LIT stability diagram in the plane (a_x, q_x) is shifted along the a_x axis by the negative value $-(4zekU_e)/(mz_0^2\Omega^2)$ for both radial directions, in comparison with the QMF stability diagram.[10] However, this shift is not significant when $z_0 > r_0$, as it is the case for the LITs used in this study.

Furthermore, strong field non-linearities exist at both ends of the LIT, inducing high-order coupling terms neglected in Eqn. (3).[11] For instance, assuming that the potential has a positive mirror symmetry with respect to the plane $z = 0$, this potential can be approximated at $x = y = 0$ by the following polynomial limited to the even-order terms:

$$\Phi_{DC}(0,0,z) = \sum_{p=0}^{+\infty} a_{2p}\frac{z^{2p}}{z_0^{2p}} \qquad (4)$$

where a_{2p} is a constant value in volts. As a consequence, generally in a real trap, the stability

diagram depends also on the initial conditions of confined ions (for instance, for a 3D quadrupole trap[12]). In other words, each ion has its own stability diagram.

The traps used as mass analyser in portable devices are normally of reduced size with simplified geometry, *e.g.* the cylindrical and rectilinear ion traps.[13] In our case, the LIT comprises four hyperbolic rods and two end-cap lenses. It is coupled to an open EI ion source by means of a set of lenses to inject the ions axially into the interior of the LIT. The four hyperbolic rods are fabricated by digital light processing (DLP LIT) using a novel polymer material and electroplating process. Low outgassing, long electrode lifetime and high voltage stability have been measured.[14]

For mass analysis, the LIT uses a Non Scanning Mode (NSM).[15] With NSM, the trap is operated close to the apex of the stability diagram in order to have mass selectivity. The NSM sequence refers to a series of the following stages achieved by switching potentials applied to the electrodes: (1) creation and injection of ions created in the EI source towards the LIT, (2) mass-selective ion confinement in the LIT at fixed trap operating point and (3) total ejection of the ions toward the detector. Only three or four ion fragments with different mass-values ranging over few hundreds are targeted when analysing a single compound. As a consequence, a succession of three or four NSM sequences (one sequence per ion fragment) reduces analysis time compared to the mass-scanning mode over a large mass range.[15] However, a set of appropriate values of the pair (U_0, V_0) can be chosen in the vicinity of the apex to produce the mass spectral peak associated with the target ion.

The mass spectrometer portability requirement introduces physical constraints: the electronic control unit (ECU) must be simple and, ideally, of low weight/cost. It is much easier to switch on/off quickly the DC voltages than the RF confinement voltage. As a consequence, it was decided to switch only DC potentials to move the operating point of the LIT during the injection and confinement stages. Both injection and trapping efficiencies in a LIT can be improved by using a He buffer gas, the effectiveness of collisional cooling depending on the gas pressure, the ion and gas masses, the collisional cross section of the ion, and the distance travelled by the ion. [6, 11, 16-19] The sensitivity enhancement has been recently demonstrated in the experimental device by adding helium buffer gas. [14]

In this work, the performance limitations (*i.e.* the number of injected and confined ions, and mass resolution) of the mass analyser must be estimated by simulation in these non-optimal operating conditions and in the absence of collisions. The maximal trajectory (radial/axial) excursions of the confined ions have to be determined for a mass-selective operating point, taking into account the non-linearity of the trap.

SIMULATION and OPERATING CONDITIONS

CPO software

The commercial software Charged Particle Optics (CPO) is used for these simulation studies.[20] In the CPO software, the device design is constructed from either predefined electrode shapes or equations. Electrical potential/field solving is done using the Boundary Element Method (BEM).[21] For the BEM, charges are distributed over the electrode surface, according to the potential applied to the electrodes. Consequently, it requires a segmentation of the electrodes into discrete intervals for computation of the charge distribution. Adaptive surface meshes become smaller where accuracy is required. However, for ion trajectory simulations, CPO software is not computationally efficient for large numbers (*e.g.* $>10^5$) of ions and simulations are excessively time consuming.

EI source/LIT coupling design

The design includes the LIT and a part of an open Electron Ionisation ion source with the coupling lenses. As simulation concerns only ion trajectories, the ion source can be limited to the ion cage fixed on the ion extraction lens and biased at the same potential $U_7 = U_8 = 3$ V (Fig. 1). The other coupling lenses with the LIT are denoted as the focusing and decelerating lenses, biased at U_6 varying and $U_5 = 0$ V, respectively. For the same device, an optimised coupling was described earlier in reference.[15] Here, a typical coupling using lenses separated by the same distance (1 mm) and having same apertures (1 mm in radius) is used.

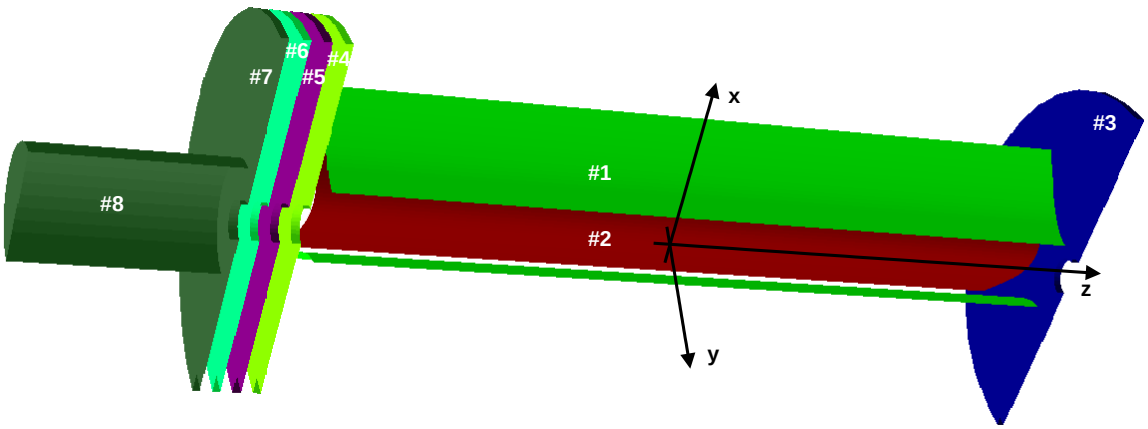

Figure 1. Design of open Electron Ionisation source/LIT coupling. Electrode #1: hyperbolic rods of x-electrodes; electrode #2: hyperbolic rods of y-electrodes; electrode #3: exit lens; electrode #4: entrance lens; electrode #5: decelerating lens; electrode #6: focusing lens; electrode #7: extraction lens; and electrode #8: ion cage.

The LIT is composed of four hyperbolic rods set parallel to each other in the z-direction and

two lenses denoted as entrance and exit lenses which are biased at DC potentials U_4 and U_3, respectively. The four hyperbolic rods of the LIT are truncated at $3r_0$ and located at $r_0 = 2$ mm. Different LIT lengths are used with $2z_0$ the length of the rods varying from 20 to 60 mm, the LITs being then denoted as LIT-20 to LIT-60, respectively.

Electrode segmentation

The effect of non-ideal segmentation is shown in Fig. 2. For this, the design comprises only the four hyperbolic rods and the two end-cap electrodes of the LIT. The four rods are biased at 0 V, while the two-end cap electrodes are held at 40 V. The potential $\Phi_{DC}(0,0,z)$ is computed for different segmentations (or meshing) of the electrodes.

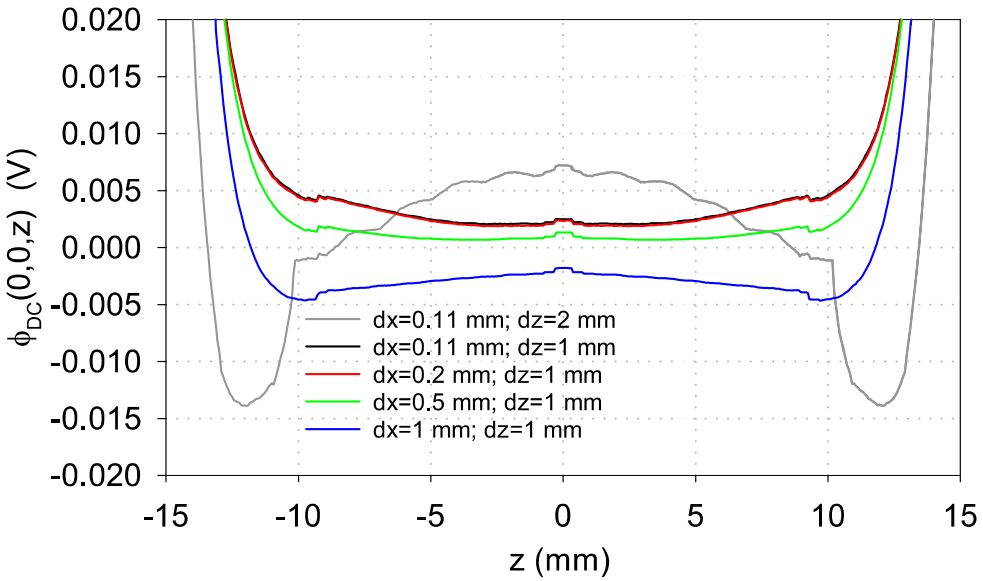

Figure 2. Potential in the LIT $\Phi_{DC}(0,0,z)$ according to the electrode segmentation, with the four hyperbolic rods biased at 0 V and the two-end caps held at 40 V.

The expected potential curve has maximal values at both ends and a minimal value in the centre of the LIT according to the polynomial development of Eqn. (4). The increase of the radial segmentation (from $dx = 0.2$ to 0.1 mm) does not change the potential curve significantly. The best fit with the potential computed by CPO is obtained with the electrode segmentation: $dx = 0.2$ and $dz = 0.1$ mm, for the smallest number of segments in order to reduce the computation time of the electric field/potential.

Initial ion drawing in the ion cage

It is assumed that an effusion from a gas cylinder forms the beam of neutrals, which is placed just in

front of the ion cage. As a consequence, the ion positions are uniformly drawn in the volume of the cylinder defining the ion cage. The ion velocities are mainly distributed along the z-direction according to a cosine law and depend on the room temperature and mass of the particle. The initial number of ions is no more than 100 (when confinement is needed) or 500 (for ion injection studies), due to long trajectory computation times by CPO. Whatever the number of ions, it is ensured that the uniform drawing sequence used is representative of a mean value issued of some tens of different drawing sequences.

Potentials applied to the hyperbolic rods

The same instant of creation ($t = 0$) is chosen for all of the ions. To take into account the temporal variations of the applied potentials, simulations are performed at different initial phases (at $t = 0$) of the RF confinement field. So, the applied RF potential must be written as: $V(t) = V_0 \cos(\Omega t + \varphi)$. Four different values of the initial phase of the RF voltage are chosen: $(j/4)2\pi$ with $j = 0 \ldots 3$. Only two values are necessary (*i.e.* $j = 0$ and 1) for the configuration No. 1 with regard to symmetry, assuming that the drawings are statistically the same in the x- and y-directions, and similar results are obtained in both x- and y-directions. All the results involving RF potentials are then averaged over those phase values.

The theoretical potential values $U_{0,apex}^{QMF}$ and $V_{0,apex}^{QMF}$ for the apex of the principal stability diagram of QMF are calculated for the confinement potential configurations No. 1 and No. 2 from the relations:

$$U_{0,apex}^{QMF} = \frac{0.237 r_0^2 \Omega^2}{8e} \times \frac{m}{z}$$
$$V_{0,apex}^{QMF} = \frac{0.707 r_0^2 \Omega^2}{4e} \times \frac{m}{z} (\text{configuration No. 1}) \qquad (5)$$
$$V_{0,apex}^{QMF} = \frac{0.707 r_0^2 \Omega^2}{2e} \times \frac{m}{z} (\text{configuration No. 2})$$

with $\Omega / 2\pi = 1$ MHz.

Non-scanning operating mode sequences

In the first simulation work, the ion manipulation was performed by switching only the DC potentials applied to the entrance and exit lenses[15]. During injection, the LIT was operated in the non-scanning mode with the confinement potentials applied to the rods. This sequence was implemented for simplicity of manufacture, but it leads to constant DC potentials applied to the electrodes during the injection stage. In addition, the ions crossing an instability zone between the lens and the trap are subject to coupling fields between the axial and radial directions, reducing the

injection efficiency.

The issue at injection is the same as with a mass filter. Typically, the ion source is adapted to a mass filter by means of an entrance lens having a smaller inner diameter than the inner diameter of the filter. The transmission efficiency improvement for this case was demonstrated by Brubaker and Tuul.[22] Later, the filter acceptance was examined in term of phase space dynamics by Dawson.[23, 24] In 1968, Brubaker proposed the use of a pre-filter operating in a RF only mode (*i.e.* with $U_0 = 0$) to greatly increase the number of injected ions. [25, 26]

The injection efficiency is then reduced when a DC potential is applied to the rods. As a consequence, in this work another sequence is proposed. In the NSM sequence No. 2, the DC confinement potential is applied only during the confinement stage and switched to zero during the injection and ejection stages (RF only mode).

CPO trajectory computation and data treatment

The points of the ion trajectories are computed at a constant time-step of 2×10^{-7} s, which is much lower than the period of the RF confinement voltage.

The points of a single trajectory computed at a constant time-step corresponds to ions created in the source with the same initial positions and velocities at different instants separated by the computation time-step. Taking into account different ion trajectories, corresponding to different initial positions and velocities in the source, the set of computed trajectory points can be representative of the ion distribution inside the LIT at steady state, *i.e.* when the number of injected ions remains constant after an injection time denoted as the minimum injection time. As a consequence, the number of computed points of all the trajectories is representative to the number of injected ions. From these points, it is also possible to calculate the ion distributions according to positions and velocities.

RESULTS AND DISCUSSION

Characterisation of ion beam entering the LIT

The characterisation of the beam of ions entering the LIT is performed with 500 ions (mono-charged) of m/z 50, 100 and 300, initially created in the ion cage, and by biasing at zero the LIT electrodes. The number of ions passing through the entrance lens and the maximal radial dispersion $dr_{\max}$ of the ion beam measured at the LIT rod entrance at -20 mm are calculated. $dr_{\max}$ is a reliable indicator of the divergence of the ion beam as the LIT is a field-free region, so that the ions in the LIT keep their initial radial and axial velocities at entrance lens aperture (Fig. 3).

The total variation in the fraction of ions passing the entrance lens as a function of U_6 does not depend on m/z, while it slightly increases from 70 to 75 % for U_6 varying from -50 to 110 V. The radial dispersion at -20 mm does not depend on m/z (Fig. 3). It is equal to the radius of the entrance lens aperture for $U_6 = -50$ V and diminished until 0.6 mm for $U_6 = -110$ V.

The influence of the radial dispersion on the number of confined ions will be tested in the following sections by using these two values of U_6.

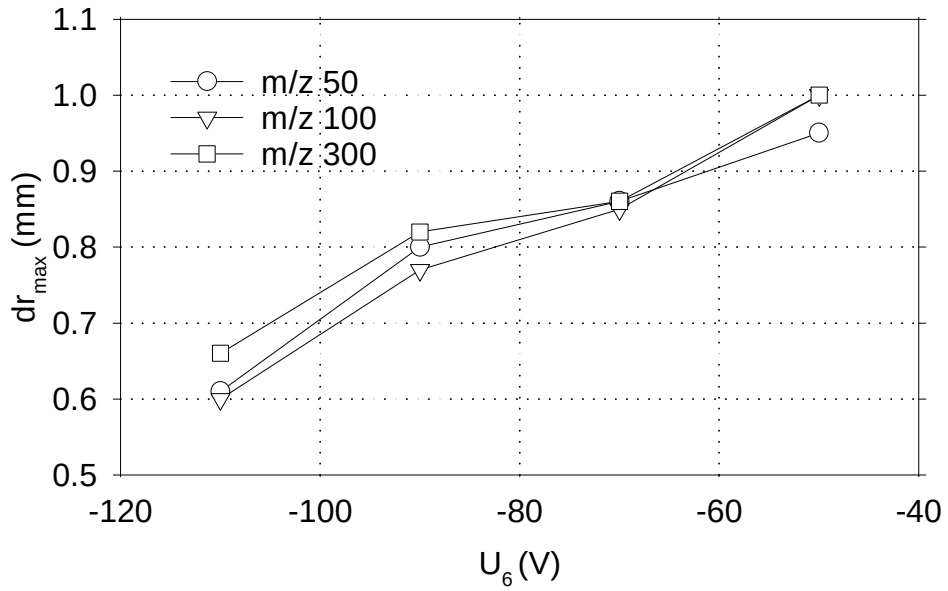

Figure 3. Maximal radial dispersion of the ion beam at LIT entrance at -20 mm, according to the potential U_6 for $m/z = 50$, 100 and 300.

Number of injected ions

100 ions of m/z 100 are injected into the LIT with the RF potentials applied to the hyperbolic electrodes according to the potential configurations No. 1 and 2, the NSM sequences No. 1 and 2, and with the DC potentials $U_3 = 20$ and 40 V and $U_4 = 0$ V applied to the exit lens and entrance lens, respectively. The number of injected ions (*i.e.* the number of ions present in the LIT at steady state) is computed from the number of points of the ion trajectories inside the LIT (Table 2).

As expected, the potential U_3 giving the location of the turn around axial location in the LIT has a weak influence on the number of injected ions. The potential configuration No. 1 always leads to the greatest number of injected ions, about 20 %, and throughout. Between $U_6 = -50$ and -100 V, a difference of 20-25 % is noticed in favour of the value giving the most collimated ion beam, *i.e.* $U_6 = -110$ V. The NSM sequence No. 1 has poor injection efficiency (10 %) in comparison

with the SIM sequence No. 2. Reducing the value of U_0 at the half-value increases the fraction of ions passing the entrance lens to 70 %. With the NSM sequence No. 1, no ions reach the initial entrance lens.

Ion distribution in the radial direction during injection

The radial position and velocity distributions, at steady state of the injection stage, are calculated from the points of the ions trajectories in the LIT computed at a constant time-step (Fig. 4).

The distribution of ions in the radial plane is not cylindrical: it has a diamond-like shape. The shape of the radial distributions (in position and velocity) is more stretched around zero than a Gaussian function. The distribution is wider along the main direction (x- or y-direction) than along the asymptotic direction of the equipotential lines in the radial plane (x_{asy}). With the potential configuration No. 1, the radial position distribution is less dispersed with $U_6 = -110$ V. In general, with the potential configuration No. 2, the radial position distribution is larger than with the potential configuration No. 1.

Ion distribution in the axial direction during injection

With the same simulation data and treatment, the distributions in position and velocity of ions in the axial direction at steady state of the injection stage are plotted in Fig. 4.

The ions are quasi-uniformly distributed in the z-direction except close to the exit lens, where they decelerate and move back towards the entrance lens after which the number of ions increases. With the potential configurations No. 2, an ion loss (about 25 %) is observed at the LIT entrance over a region of 6 mm. As previously shown, the number of injected ions is greater with the potential configuration No. 1, and also with $U_6 = -110$ V.

The potential configuration No. 1 leads to narrow distributions of axial velocities for ions going towards the exit lens (positive velocity distribution) as well as for ions coming back to the entrance lens (negative velocity distributions), with the same dispersion and ion quantities when comparing the areas of these two velocity distributions. With the potential configuration No. 2, the axial velocity distribution is larger, due to the time-varying potential in the centre of the trap. The mean value of all the distributions is about 2400 m/s corresponding to the potential energy of the ion cage biased at 3 V.

The potential applied to the end-caps must be chosen according to the maximal value of the axial velocity distribution. U_3 must be greater than 4.7 and 13 V, as 3000 and 5000 m/s are the maximum axial velocities measured in the case of the confinement potential configuration No. 1 and No. 2, respectively, with the ion cage biased at 3 V.

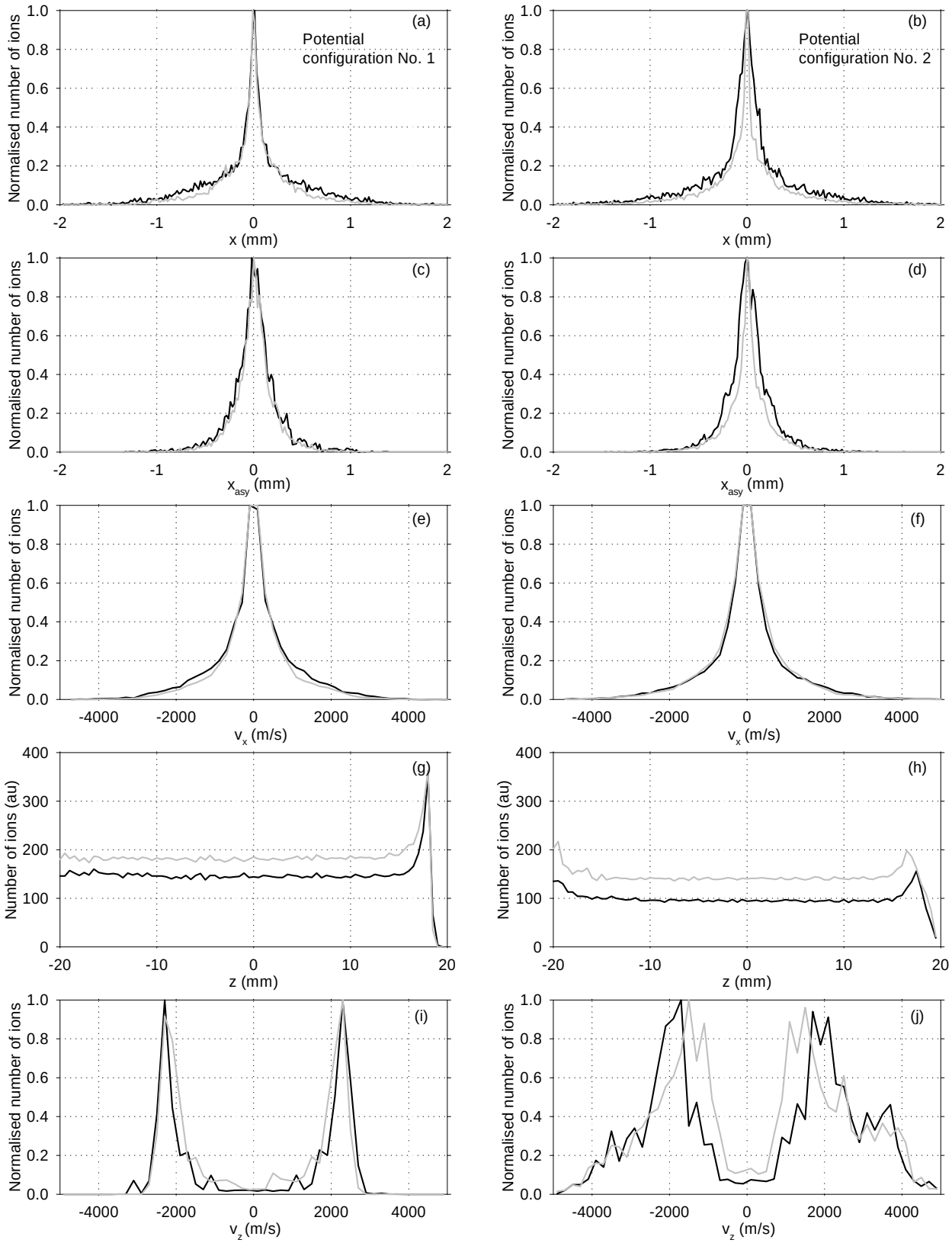

Figure 4. Ion distributions in LIT-40 at injection stage for potential configuration No. 1 (left curves) and No. 2 (right curves). The number of ions is normalised so that the maximum of the distribution equals 1. (a) and (b): Normalised ion distribution versus x-direction; (c) and (d):

Normalised ion distribution versus asymptotic direction of the equipotential lines in the radial plan (x_{asy}); (e) and (f): Normalised ion distribution versus x-velocity; (g)-(h) Ion distribution versus z-direction; (i) and (j): Normalised ion distribution versus z-velocity. The other simulation conditions are: $U_6 = -50$ (full line) and -110 V (grey line) for NSM sequence No. 2, $U_3 = 20$ V and ions of m/z 100.

Minimal injection time

The number of injected ions versus the injection time is calculated from a single point of time of creation in the ion cage. The curves plotted in Fig. 5 represent the mean values of the number of injected ions calculated for different initial phases of the RF confinement potential. The number of injected ions diminishes with time, as ion creation occurs at a single point in time. The minimal injection time is defined when the number of ions is zero, corresponding also to the maximal number of injected ions when ion creation is continuous.

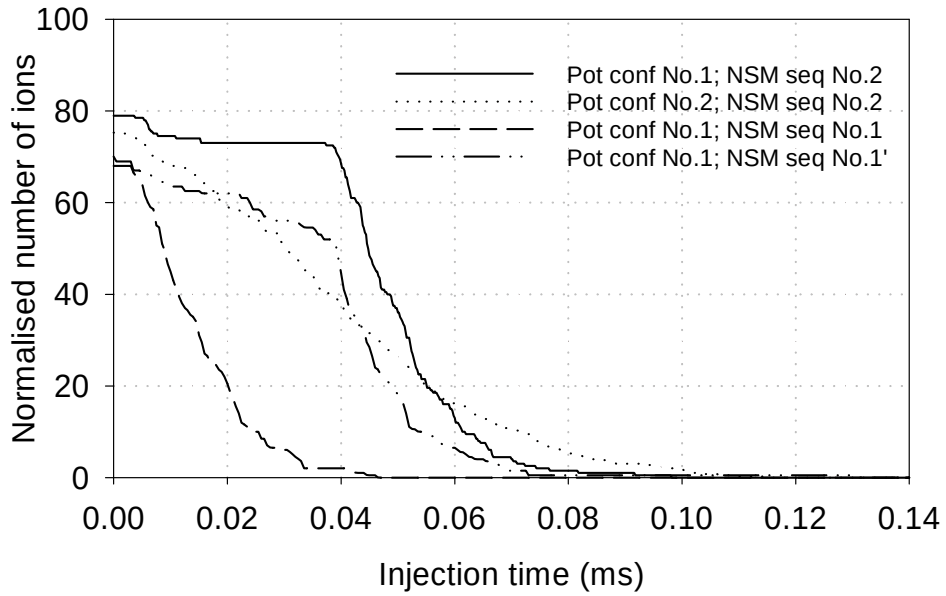

Figure 5. Normalized ion distribution versus time for a punctual time of creation in the ion source, according to potential configurations No. 1 and No. 2 and NSM sequences No. 1 and No. 2 with potentials $U_3 = 20$ V and $U_6 = -110$ V, and ions of m/z 100.

With the potential configuration No. 1 and NSM sequence No. 2, two ion losses are observed: the first decrease corresponds to an effective ion loss during injection when ions go towards exit lens, while the second one is mainly attributable to the ions reaching the entrance lens at different times according to their axial velocity. Due to the large axial velocity distribution, a quasi-linear decrease is observed with the potential configuration No. 2 and NSM sequence No. 2. The minimal

injection time deduced from the curves of Fig. 5 is almost equal to 120 µs. With the potential configuration No. 1 and NSM sequence No. 1, the ion loss occurs mainly when the ions go towards the exit lens. Few ions can go back close to the exit lens, but they experience the strong non-linearities in this region of the LIT, consequently they are lost very quickly after return. No ions reach the entrance lens when they turn around. With the potential configuration No. 1, a few number of ions has been measured (10 %, see Table 2) and the position and velocity distributions of the cloud at injection will lead to non confinable ions, as the remaining ions are lost as soon as they experience non-linearities at the exit lens during the injection stage.

Apex value of the principal stability diagram of LIT

The NSM operating mode requires to know accurately the potential values $U_{0,apex}^{LIT}$ and $V_{0,apex}^{LIT}$ to be applied to the x- and y-electrodes to operate the LIT at the apex of the stability diagram during the confinement stage.

Let us consider a single ion of m/z 100 confined for different initial conditions in radial and axial positions, and the initial velocities equal to zero. The confinement potentials are applied to the rods according to the configuration potential No. 1 and the two end-caps are biased at $U_3 = U_4 = 20$ V. V_0 is chosen equal to $V_{0,apex}^{QMF}$ and U_0 is varied with steps of 0.1 V for values lower than $U_{0,apex}^{QMF}$. The highest value of U_0 at which the ion is confined during at least 1 ms is denoted as $U_{0,apex}^{LIT}$. By this way, the apex of the stability diagram takes into account, not only the stability of the radial motion in the centre of the trap, but also integrates the non-linear resonances at both ends close to end-cap lenses: even ions having a stable motion with large excursion can be lost due to energy exchange between the radial and axial directions that occurs at both ends of the LIT.

The computed values of $U_{0,apex}^{LIT}$ are plotted *versus* $z(0)$ Fig. 6 according to different initial radial positions and LIT lengths. $z(0)$ can be also considered as an approximation of the maximal excursion of the ion axial trajectory, as initial axial velocity is zero. The horizontal dashed line represents the theoretical QMF apex value of the principal diagram, $U_{0,apex}^{QMF}$, which does not depend on initial conditions of ion. All the LIT apex values are lower than the QMF apex value. They remain constant until $z(0) < z_{Mconf}$, they then decrease until the maximal excursion reaches the end of the LIT. z_{Mconf} is representative of the maximal excursion of the axial trajectory for the ion to be confined, if the trap is operated at value of the plateau of $U_{0,apex}^{LIT}$. The coupling between the axial and radial directions can be neglected when the excursion of the axial trajectory remains lower than z_{Mconf}. The value of z_{Mconf} decreases with the increase of the initial radial positions. The size of the

LIT does not significantly modify this value. z_{Mconf} increases with the size of the LIT.

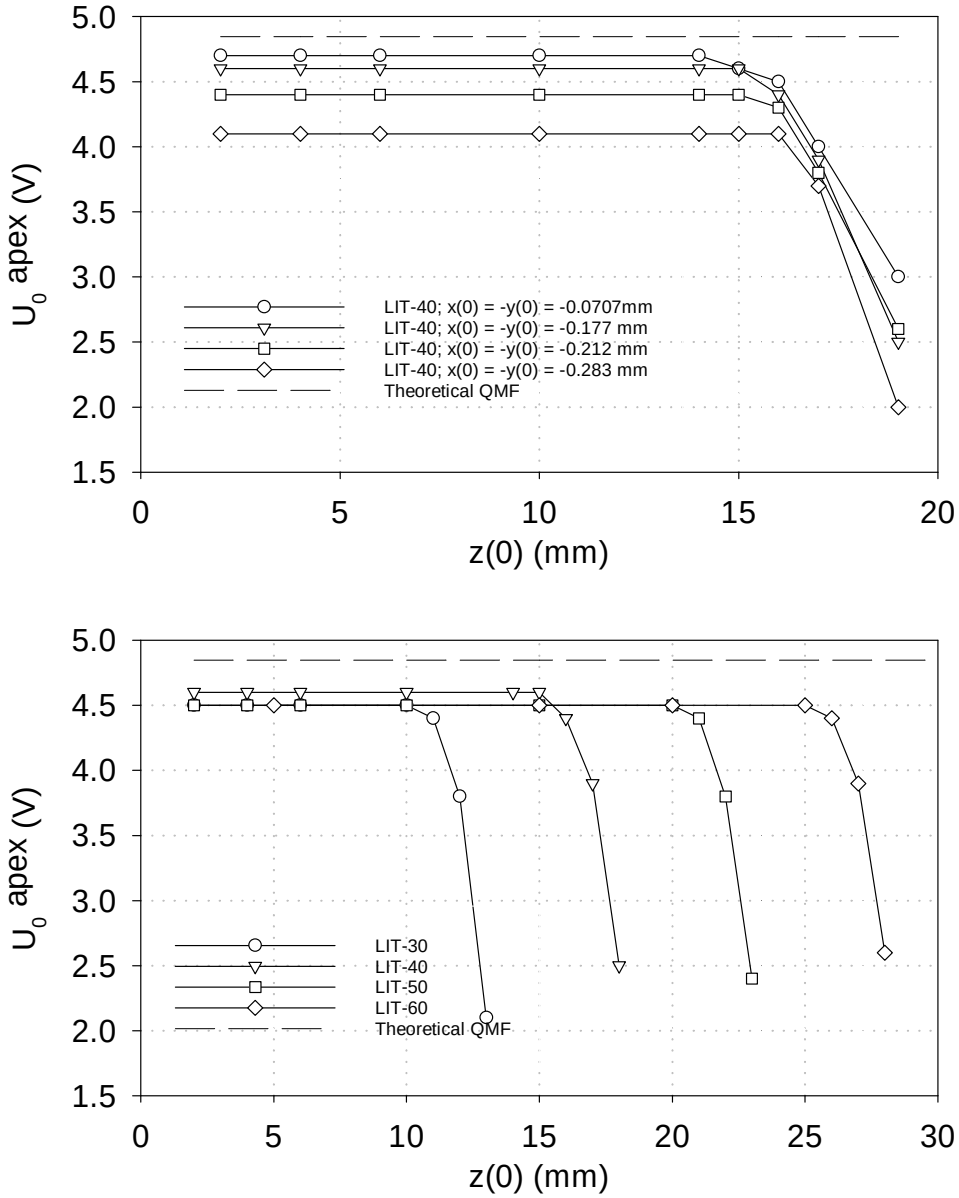

Figure 6. Apex value ($U_{0,apex}^{LIT}$) of the LIT principal stability diagram of a single ion of m/z 100 versus $z(0)$ (or maximal axial trajectory excursion): (top curve) according to different initial radial positions (or radial trajectory excursion) with LIT-40 and (bottom curve) according to LIT lengths with $x(0) = -y(0) = -0.177$ mm and $U_3 = U_4 = 20$ V. The theoretical value of the corresponding QMF apex ($U_{0,apex}^{QMF}$) is represented by the dashed line.

Axial trajectory excursion effects on confinability close to the stability diagram apex

If the trap is operated at the value of the plateau of $U_{0,apex}^{LIT}$, two issues must be addressed to

increase both sensitivity and resolution. On one hand, the ion cloud occupies almost the whole of the axial positions at injection, so that ions having trajectory excursions larger than z_{Mconf} are lost during confinement. On the other hand, due to the radial position distribution of the ion cloud at injection stage, a compromise must be found between mass-selectivity and number of confined ions. In either case, the initial position distributions of ions must be reduced prior to the confinement stage.

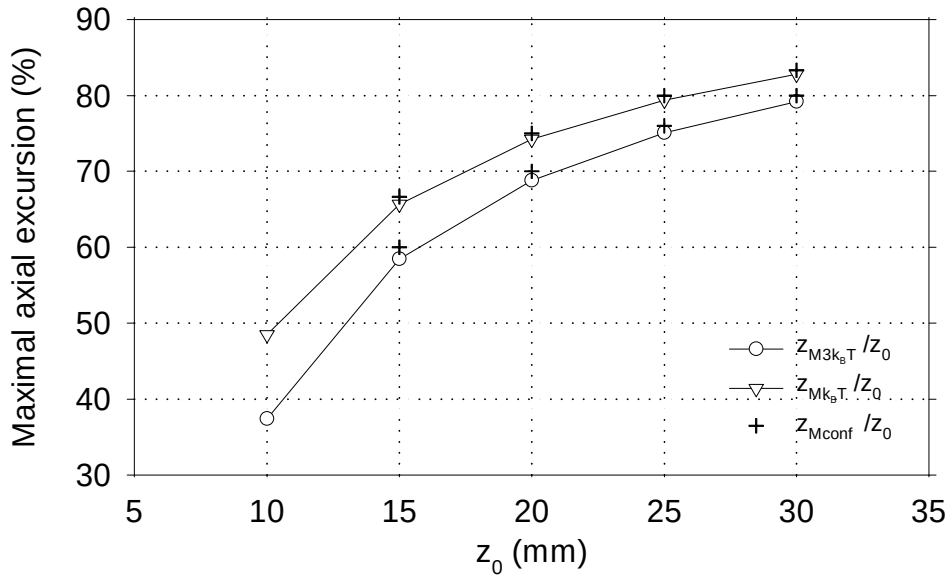

Figure 7. Maximal axial excursion of a single ion confined in different LIT lengths: (+) z_{Mconf}/z_0, when the trap is operated at the plateau of $U_{0,apex}^{LIT}$; (∇) z_{Mk_BT}/z_0 when the potential well depth equals k_BT; and (○) z_{M3k_BT}/z_0 when the potential well depth equals $3k_BT$, for a single ion of m/z 100.

The normalised values z_{Mconf}/z_0 (the values founded in bottom curve of Fig. 6) are plotted in Fig. 7 as a function of z_0, the LIT length. For each LIT length, the two crosses indicate the maximal and minimal limits of z_{Mconf}/z_0, as the value of U_0 is varied in steps. The axial extent of the confined ion cloud occupies 80 % of the axial direction for LIT-60 and only 60 % for LIT-30.

Let us calculate the maximum axial excursion of confined ions for two values of the axial potential well depth regarding the value of k_BT, with T the temperature (K) of a He buffer gas, for instance, and k_B the Boltzmann constant (J/K). When the axial potential well depth is equal to k_BT and $3k_BT$, the maximal trajectory excursions z_{Mk_BT} and z_{M3k_BT} are deduced from the

equations $\Phi_{DC}(0,0,z_{Mk_BT}) = k_BT$ and $\Phi_{DC}(0,0,z_{M3k_BT}) = 3k_BT$, respectively, with potential values computed from CPO. The normalised values z_{Mk_BT}/z_0 and z_{M3k_BT}/z_0 are then plotted in Fig. 7 as a function of z_0. The required values of z_{Mconf} match those of z_{Mk_BT} and z_{M3k_BT}. As a consequence, if He buffer gas is used [6, 11, 16, 17], efficient ion cooling can reduce the axial dimension of the injected ion cloud so that very few ions are lost in the axial direction, when the trap is operated at the value of the plateau of $U_{0,apex}^{LIT}$.

Radial trajectory excursion effects on confinability and resolution close to the stability diagram apex

The plateau of $U_0 = U_{0,apex}^{LIT}$ must be determined more accurately according to initial radial positions. The location of the highest limit of confinement (or the "iso-beta line $\beta_y = 0$") of three mass-over-charge ratios $m/z = 99$, 100 and 101 is calculated by varying U_0 with steps of 0.01 V according to different initial radial positions (Fig. 8). The initial axial position is chosen lower than z_{Mconf}.

With the lowest initial radial position, $x(0) = -y(0) = -0.001$ mm, the LIT stability diagram has the greatest area and tends to the QMF stability diagram. For a same value of V_0 and for the same initial radial conditions, the iso-beta lines of each m/z are shifted down by the same value of U_0. For instance, for $m/z = 100$ and initial radial positions $x(0) = -y(0) = -0.0707$ mm, the iso-beta $\beta_y = 0$ line is at $U_0 = 4.79$ V instead of 4.85 V for the QMF for $V_0 = 28.89$ V. The iso-beta line of $m/z = 100$ for $x(0) = -y(0) = -0.0707$ mm matches the iso-beta line of $m/z = 101$ for $x(0) = -y(0) = -0.001$ mm.

As a consequence, a mass separation of one unit can be then achieved with a cloud of ions having initial radial positions within a radius of 0.1 mm around the z-direction. However, only 13 % of the injected ions will be confined (value calculated by a 3D integration of the ion distribution at injection given in Fig. 3). To increase the number of confined ions, the value of U_0 can be diminished but the mass separation is degraded. Therefore, collisional cooling is necessary to reduce the radial dispersion of the injected ions.

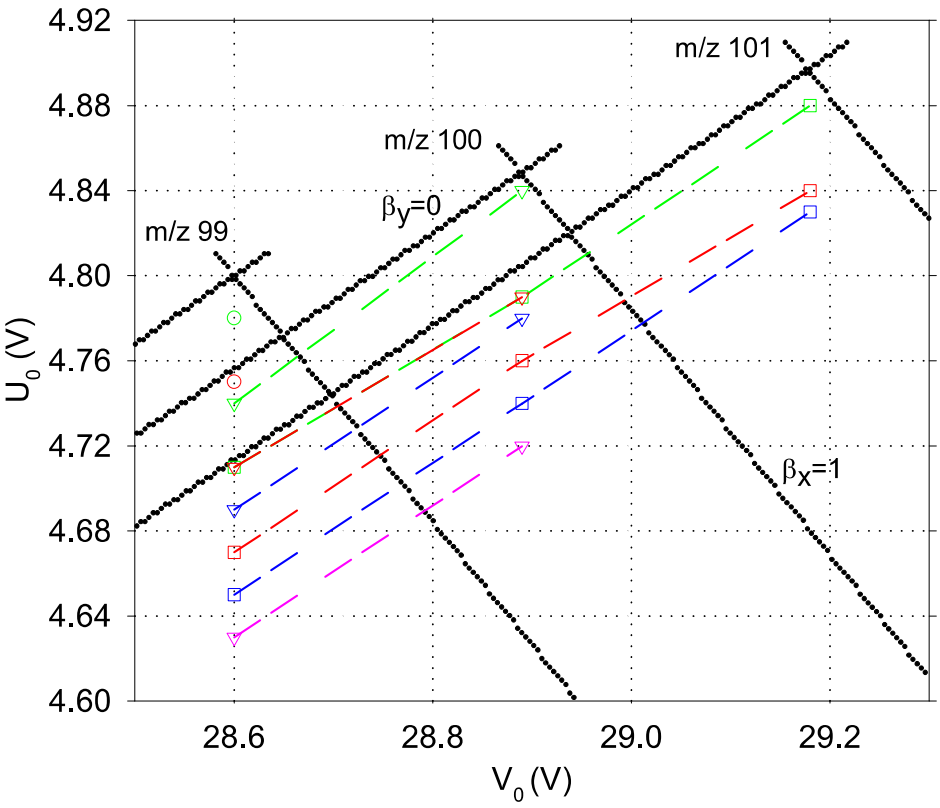

Figure 8. Principal stability diagram of QMF close to apex for $m/z = 99$, 100 and 101. "Iso-beta lines $\beta_y = 0$" of LIT-40 stability diagram for $m/z = 99$ (○), 100 (∇) and 101 (□), and different initial radial positions: (green) $x(0) = -y(0) = -0.001$ mm; (red) $x(0) = -y(0) = -0.0707$ mm; (bleu) $x(0) = 0$ mm and $y(0) = -0.1$ mm; (purple) $x(0) = 0$ mm and $y(0) = -0.15$ mm. $U_3 = U_4 = 20$ V.

CONCLUSIONS

During the injection stage, it is essential to switch the DC confinement voltage to zero. Even though the potential configuration No. 1 leads to a greater number of ions (about 20 % greater than with the potential configuration No. 2), the potential configuration No. 2 has been chosen in the first prototype, since the potential configuration No. 1 involves two out of phase RF supplies. To operate the trap close to the apex of the stability diagram (non-scanning operating mode) with a mass-to-charge resolving power of one unit at least and the greatest number of confined ions, the size of injected ion cloud must be reduced as much as possible.

Collisional cooling can be used to optimise the efficiency when the trap is operated in an RF mode. As a consequence, the present sequence of the NSM mode should be modified. A cooling stage should be added after injection stage with both end-caps biased at a positive DC value for the axial confinement potential and the DC confinement potential maintained at zero volts for the radial

confinement potential applied to the four rods. It will be then necessary to determine the optimal cooling time prior to moving the DC potential from zero towards the apex potential value. This work will be based on previous ones where the mass-selective isolation of ions stored in a quadrupole ion trap (3D) has been studied. [27, 28]

Investigations of the ion collisional cooling are on-going using two different simulation approaches. The first one allows us to produce the position and velocity distributions of an ion cloud at an equilibrium state using the temporal invariance method. This technique has been recently improved for simulation of a 3D RF ion trap by the use of both a control model associated to the investigated device and no Gaussian ion distribution functions.[29] A control model is being developed to apply this method to linear ion traps. The second approach is more standard. It employs the BEM method to compute the potential and the trajectory computations of the ion cloud including collisional effects. It is faster than CPO, and useful for simulation of a large numbers ion ensemble.

ACKNOWLEDGMENTS

This research work received funding from the European Community's Seventh Framework Programme managed by the Research Executive Agency (FP7/2007-2013) under grant agreement 285045.

REFERENCES

[1] M. Welling, R. I. Thompson, H. Walther. Photodissociation of MgC60+ complexes generated and stored in a linear ion trap. *Chemical Physics Letters* **1996**, *253*, 37.

[2] M. Welling, H. A. Schuessler, R. I. Thompson, H. Walther. Ion/molecule reactions, mass spectrometry and optical spectroscopy in a linear ion trap. *International Journal of Mass Spectrometry and Ion Physics* **1998**, *172*, 95.

[3] M. W. Senko, J. C. Schwartz, A. E. Schoen, J. E. P. Syka. in *Proceedings of the 48th ASMS Conference on Mass Spectrometry and Allied Topics*, Long Beach, CA, **2000**.

[4] M. Senko. Linear quadrupole mass spectrometer. US Patent: US6403955 B1. **2002**.

[5] J. C. Schwartz, M. W. Senko, J. E. P. Syka. A two-dimensional quadrupole ion trap mass spectrometer. *Journal of the American Society for Mass Spectrometry* **2002**, *13*, 659.

[6] J. W. Hager. A new linear ion trap mass spectrometer. *Rapid Communications in Mass Spectrometry* **2002**, *16*, 512.

[7] F. A. Londry, J. W. Hager. Mass selective axial ion ejection from a linear quadrupole ion trap. *Journal of the American Society for Mass Spectrometry* **2003**, *14*, 1130.

[8] A. Drakoudis, M. Söllner, G. Werth. Instabilities of ion motion in a linear Paul trap. *International Journal of Mass Spectrometry* **2006**, *252*, 61.

[9] D. A. Tabor, V. Rajagopal, Y.-W. Lin, B. Odom. Suitability of linear quadrupole ion traps for large Coulomb crystals. *Applied Physics B* **2012**, *107*, 1097.

[10] M. Drewsen, A. Brøner. Harmonic linear Paul trap: Stability diagram and effective potentials. *Physical Review A* **2000**, *62*, 045401.

[11] D. J. Douglas, A. J. Frank, D. Mao. Linear ion traps in mass spectrometry. *Mass Spectrometry Reviews* **2005**, *24*, 1.

[12] A. Janulyte, Y. Zerega, M. Carette. Harmful influences of confinement field non-linearities in mass identifying for a Fourier transform quadrupole ion trap mass spectrometer: Simulation studies. *International Journal of Mass Spectrometry* **2007**, *263*, 243.

[13] A. S. Scott, C. M. Christopher, S. Qingyu, J. N. Robert, R. G. Cooks, O. Zheng. in *Practical Aspects of Trapped Ion Mass Spectrometry, Volume IV*, CRC Press, Boca Raton, **2010**, pp. 169.

[14] B. Brkic, S. Giannoukos, N. France, R. Murcott, F. Siviero, S. Taylor. Optimized DLP linear ion trap for a portable non-scanning mass spectrometer. *International Journal of Mass Spectrometry* **2014**, *369*, 30.

[15] B. Brkic, S. Giannoukos, N. France, A. Janulyte, Y. Zerega, S. Taylor. Modeling of an ion source lens system for sensitivity enhancement in a non-scanning linear ion trap. *International Journal of Mass Spectrometry* **2013**, *353*, 36.

[16] B. A. Collings, J. M. Campbell, D. Mao, D. J. Douglas. A combined linear ion trap time-of-flight system with improved performance and MSn capabilities. *Rapid Communications in Mass Spectrometry* **2001**, *15*, 1777.

[17] Y. Hashimoto, H. Hasegawa, I. Waki. Dual linear ion trap/orthogonal acceleration time-of-flight mass spectrometer with improved precursor ion selectivity. *Rapid Communications in Mass Spectrometry* **2005**, *19*, 1485.

[18] W. Xu, Q. Song, S. A. Smith, W. J. Chappell, Z. Ouyang. Ion Trap Mass Analysis at High Pressure: A Theoretical View. *Journal of the American Society for Mass Spectrometry* **2009**, *20*, 2144.

[19] Q. Song, W. Xu, S. A. Smith, L. Gao, W. J. Chappell, R. G. Cooks, Z. Ouyang. Ion trap mass analysis at high pressure: an experimental characterization. *Journal of Mass Spectrometry* **2010**, *45*, 26.

[20] F. H. Read, N. J. Bowring. The CPO programs and the BEM for charged particle optics. *Nuclear Instruments and Methods in Physics Research Section A: Accelerators, Spectrometers, Detectors and Associated Equipment* **2011**, *645*, 273.

[21] F. H. Read, A. Adams, J. R. Soto-Montiel. Electrostatic cylinder lenses. I. Two element lenses. *Journal of Physics E: Scientific Instruments* **1971**, *4*, 625.

[22] W. M. Brubaker, J. Tuul. Performance Studies of a Quadrupole Mass Filter. *Review of Scientific Instruments* **1964**, *35*, 1007.

[23] P. H. Dawson. A detailed study of the quadrupole mass filter. *International Journal of Mass Spectrometry and Ion Physics* **1974**, *14*, 317.

[24] P. H. Dawson. The Acceptance of the Quadrupole Mass Filter. *International Journal of Mass Spectrometry and Ion Physics* **1975**, *17*, 423.

[25] W. M. Brubaker. in *Advances in Mass Spectrometry, Vol. 4* (Ed.: E. Kendrick), The Institut of Petroleum, London, **1968**, pp. 293.

[26] P. H. Dawson. Fringing Fields in the Quadrupole Mass Spectrometer. *International Journal of Mass Spectrometry and Ion Physics* **1971**, *6*, 33.

[27] R. E. March, F. A. Londry, R. L. Alfred, A. M. Franklin, J. F. J. Todd. Mass-selective isolation of ions stored in a quadrupole ion trap. A simulation study. *International Journal of Mass Spectrometry and Ion Physics* **1992**, *112*, 247.

[28] R. E. March, M. Tkacyzk, F. A. Londry, R. L. Alfred. Mass-selective isolation of ions stored in a quadrupole ion trap. Part 2. a simulation study of consecutive isolation. *International Journal of Mass Spectrometry and Ion Physics* **1993**, *125*, 9.

[29] J. André, A. Janulyte, Y. Zerega. An historical approach to the effects of elastic collisions in radiofrequency devices and recent developments. *International Journal of Mass Spectrometry* **2015**, *377*, 355.

TABLES

Table 1. Potential applied to the hyperbolic rod x- and y-electrodes during confinement, the corresponding expression of the 2D potential inside the LIT, and of the reduced parameters of the Mathieu equation.

	Configuration No. 1	Configuration No. 2	Configuration No. 3
Potential at x-electrodes	$V(t) = U_0 + V_0 \cos \Omega t$	$-U_0$	0
Potential at y-electrodes	$-U_0 - V_0 \cos \Omega t$	$U_0 + V_0 \cos \Omega t$	$U_0 + V_0 \cos \Omega t$
$\Phi_{QMF}(x,y,t)$	$\left[U_0 + V_0 \cos \Omega t\right]\left[\frac{x^2 + y^2}{r_0^2}\right]$	$\left[-U_0 - \frac{V_0 \cos \Omega t}{2}\right]\left[\frac{x^2 - y^2}{r_0^2}\right] + \frac{V_0 \cos \Omega t}{2}$	$\left[\frac{U_0 + V_0 \cos \Omega t}{2}\right]\left[\frac{x^2 - y^2}{r_0^2}\right] + \frac{U_0 + V_0 \cos \Omega t}{2}$
Reduced parameters	$a_x = -a_y = \frac{8zeU_0}{mr_0^2\Omega^2}$ $a_x = -a_y = \frac{-4zeV_0}{mr_0^2\Omega^2}$	$a_x = -a_y = \frac{-8zeU_0}{mr_0^2\Omega^2}$ $a_x = -a_y = \frac{2zeV_0}{mr_0^2\Omega^2}$	$a_x = -a_y = \frac{4zeU_0}{mr_0^2\Omega^2}$ $a_x = -a_y = \frac{-2zeV_0}{mr_0^2\Omega^2}$

Table 2. Number of injected ions (i.e. the number of ions present in the LIT at steady state of injection stage) according to confinement potential configurations, NSM sequences and potentials U_3 and U_6. NSM sequence No. 1 refers to $U_0 = U_{0,apex}^{QMF}$ and No. 1' to $U_0 = U_{0,apex}^{QMF}/2$.

Potential configuration	NSM sequence	U_6	U_3	No. of ions
No.	No.	(V)	(V)	(%)
1	2	-50	20	81
1	2	-50	40	79
1	2	-110	20	100
1	2	-110	40	97
2	2	-50	20	54
2	2	-50	40	54
2	2	-110	20	79
2	2	-110	40	75
1	1	-110	20	10
1	1'	-110	20	70